On the formation of thrust-faults related landforms under low strain rate in Mercury's Northern Smooth Plains: A two-dimensional numerical simulation

Jingchun Xie[1,2], Chengli Huang[3,2,4] and Mian Zhang[3,4]

[1]Shanghai Astronomical Observatory, Chinese Academy of Sciences, Shanghai 200030, China
[2]School of Physical Science and Technology, ShanghaiTech University, Shanghai 201210, China
[3]CAS Key Laboratory of Planetary Sciences, Shanghai Astronomical Observatory, Chinese Academy of Sciences, Shanghai 200030, China
[4]School of Astronomy and Space Science, University of Chinese Academy of Sciences, Beijing 100049, China

Key Points:

- A new model satisfying the deduction from thin-rooted deformation is proposed to study the formation of thrust-faults in Mercury's NSP area.
- A 2-D numerical simulation is conducted, from which a surface topography well consistent with observed shortening features is obtained.
- This refined mechanical structure model of Mercury's lithosphere can be extended to three dimensions to other geological characteristics.

Corresponding author: Chengli Huang, `clhuang@shao.ac.cn`

Abstract

There are a large number of thrust-faults related landforms distributed across the Planet Mercury, which are interpreted as the result of lithospheric deformation mainly attribute to secular cooling of the planetary interior. Exploring the mechanisms for formation of thrust-faults is a key to understand the evolutionary history of Mercury. As the largest single volcanic deposit on Mercury, the northern smooth plains incubates numerous shortening features in which present particularity in their tectonic patterns and require an assumed stratified subsurface structure. In this work, we propose a thermo-dynamic model from the perspective of temperature, rheological laws and strain rate, to study the formation of the thrust-faults related landforms in the northern smooth plains of Mercury under low strain rate via two-dimensional viscoelastic-plastic numerical simulations. Our simulation starts at 3.8 billion years ago and lasts for 70 million years, resulting in a stable and concentrated high strain rate region within the crust and geomorphic consistent surface topography with typical shortening landforms. This work refines the commonly used lithospheric mechanical model of Mercury and emphasizes the importance and sensitivity of the relationship between the surface topography and the relief at the crust-mantle boundary. Future studies can be extended to higher dimensions on this basis to study the distribution, orientation and other characteristics of the thrust-faults related landforms on Mercury.

Plain Language Summary

One of the most striking features of Mercury's surface is the global distribution of shortening geological landforms. The formation and characteristics like surface topography of these tectonic features are associated with the mechanical structure of lithosphere, which is controlled by a variety of factors such as the rock's composition, ambient temperature and background strain rate. For the Mercury's northern smooth plains, there is neither satisfied lithospheric mechanical model nor numerical simulations for the formation processes of the contraction geomorphy. We present a new lithospheric mechanical model for simulation of the formation of typical shortening features at around 3.8 billion years ago in the above area via two-dimensional numerical simulation. The new model subdivides the mechanical structure of the lithosphere, allowing for a fragile layer at the shallow depth within the lithosphere beneath the northern smooth plains of Mercury, which promotes the formation of shallow-rooted shortening geomorphy. This work is tested with an open-source finite element mantle convection code, resulting in a geomorphic consistent surface relief which is well consistent with the typical shortening features observed. The proposed model can be regarded as a meaningful supplementary to the mechanical model of the lithosphere of Mercury and other terrestrial planets, worthy of further application in related research areas.

1 Introduction

Previous studies have shown that there are numerous geometries of shortening tectonic features distributed across the planet Mercury (e.g., Watters et al., 2009; Solomon et al., 2018). These structures have been widely accepted as one of the results of the shrinkage and failure of the lithosphere, mainly due to the stress caused by secular cooling of the interior (Byrne et al., 2014, 2018; Banks et al., 2015; Klimczak et al., 2019). Among them, the most common geological landforms are lobate-scarps, wrinkle ridges and high relief ridges (Watters et al., 2009; Klimczak et al., 2019). Taking the lobate-scarps as an example, they are interpreted as the manifestation of the surface-breaking thrust-faults and found to deform almost all major geological units on Mercury (e.g., Banks et al., 2015; Watters et al., 2021). The mechanisms of thrust-faults initiation on Mercury are applicable to the common frictional sliding model, reflecting the relationships between the plastic strength of the lithosphere itself and the stresses exerted by the environment, which can further provide important information for understanding the evolutionary history of Mercury (D. L. Kohlstedt & Mackwell, 2009; Klimczak, 2015; Klimczak et al., 2019).

Global maps imaged by NASA's MESSENGER spacecraft revealed that about 27% of the Mercury's surface is covered by extensive smooth plains, which contains the largest single volcanic deposit, i.e., the northern smooth plains (NSP) (Head et al., 2011; Denevi et al., 2013; Ostrach et al., 2015). Stratigraphic studies on thrust-faults related landforms found in the NSP (mainly are wrinkle ridges and lobate-scarps) classified the main style of deformation as thin-rooted, and it is suggested that this phenomenon could be due to a multilayered subsurface structure underlying the NSP (e.g., Watters et al., 2021; Byrne et al., 2014; Crane & Klimczak, 2017; Peterson et al., 2020; Watters, 2021). Additionally, relationships between the crustal thickness and mantle melting production indicated a thin crust with an average thickness of 19km beneath the NSP, thinner than earlier estimates (Padovan et al., 2015; Sori, 2018), supporting a low-degree mantle melting production scenario (Beuthe et al., 2020). More recently, Watters (2021) analyzed the relevance of the contraction strain to the crustal thickness in Mercury, and concluded that thinner crust undertakes smaller contraction strain. Let alone the background bulk strain rate (before and) at the onset of faulting has been restricted to orders of magnitude smaller than previous commonly adopted value in strength models (e.g., ductile-strength model in Zuber et al. (2010)) (Klimczak, 2015; Crane & Klimczak, 2017). Collectively, these works outline a picture of shallow depth deformation in the NSP with a thin crust under low background bulk strain rate.

In essence, the initiation of thrust-faults is controlled by rock's compositions, the ambient temperature, strain rate and rheology laws and other factors (e.g., Karato & Wu, 1993; Katayama, 2021). Given the assumptions of former factors, one can calculate the strength profile of the lithosphere to provide a rough illustration of the lithospheric mechanical structure. Applications of ductile-strength model to the old geological terrane-the intercrater plains (ICP) on Mercury suggested that the thrust-faults have formed in a mechanically homogeneous lithosphere from substantial horizontal compressive stress, allowing a maximum fault penetrate depth to 30-40km (Watters et al., 2002; Egea-González et al., 2012). However, such model can easily deduce that the entire or most of crust is homogenous and abide by brittle deformation (e.g., D. Kohlstedt et al., 1995; Byrne et al., 2018). Geological works on the shortening features in the NSP suggested that multisequence eruption of volcanic flows and the underlying megaregolith layer produced by impact events may result in mechanically heterogeneous layers at a shallow depth in the crust, facilitating deformation (Crane & Klimczak, 2017; Solomon et al., 2018; Peterson et al., 2020; Watters, 2021). Clearly, the strength model applicable to the NSP should be able to explain account for the presence of mechanical anisotropic layers in the crust or the lithosphere. Therefore, it is inappropriate to apply the ductile-strength model without improvements to the NSP. Nevertheless, the mechanism for formation of thrust-faults related landforms in the NSP is still an open and interesting question. On the other hand, there is a lack of numerical simulations aiming at the formation process of thrust-related landforms in the NSP, which can provide more richer information about the early evolutionary history of Mercury.

In this paper, we propose a thermo-dynamic model to study the formation of the thrust-faults related landforms in the NSP under low strain rate via two-dimensional viscoelastic-plastic numerical simulation. Our model subdivides the structure of the lithosphere into several mechanical discontinuous layers by introducing the semi-brittle deformation, which tends to induce strain localization at the mechanical discontinuous (Thielmann & Kaus, 2012; Schmalholz & Duretz, 2015). This work is tested with the open-source finite-element mantle convection code: Advanced Solver for Problems in Earth's ConvecTion, ASPECT (Kronbichler et al., 2012; Heister et al., 2017) `https://aspect.geodynamics.org`. Additional technical details of this paper can be found via the link provided by the Open Research section. This paper is structured as follows. First, The physical model is introduced in Section 2, next is the model configuration in Section 3. Our results are presented in Section 4, and the context of discussion is shown in Section 5, last is our conclusion in Section 6.

2 Physical Model

As for the mantle convection model, we apply an incompressible, linear Maxwell model to take viscoelasticity into account. The constitutive equation for all materials is (e.g., Moresi et al., 2003):

$$\frac{\tau}{2\eta} + \frac{\bar{\tau}}{2\mu} = \hat{D_v} + \hat{D_e} = \hat{D} \tag{1}$$

Where τ is the deviatoric stress tensor, μ is the elastic shear modulus, η is the shear viscosity, and $\bar{\tau}$ is the Jaumann corotational stress rate tensor. $\hat{D_v}$ and $\hat{D_e}$ are the viscous part and elastic component of the deviatoric strain rate tensor, respectively. For further discussion of this equation, please refer to Appendix A.

The basic equations set describing the conservation of mass, momentum and energy is given by:

$$\nabla \cdot u = 0 \tag{2}$$

$$\tau_{ij,j}^{t+\Delta t^e} - \nabla P + f_i + F_i^{e,t} = 0 \tag{3}$$

$$\rho c \frac{\partial T}{\partial t} = \frac{\partial}{\partial x_i}(k\frac{\partial T}{\partial x_i}) + H_R + H_D \tag{4}$$

Where u is the velocity, P is the pressure, and f_i is the specific body force, $F_i^{e,t}$ is the elastic force term. In Eq.(4), ρ is the density, c is the specific heat capacity, and the last three terms on the right side represent the conductive heat, radiogenic heat and viscous dissipation, respectively.

The radiogenic heat term has the following form (e.g., Michel et al., 2013):

$$H_x(t) = \rho_x \sum_i Q_i^0 0.5^{t/\mu_i} \tag{5}$$

Where x is the index which represents different geological layers, $H_x(t)$ is the heat production rate in W/m^3, ρ_x is the average density. i is the index denoting radioactive heating elements (RHEs), Q^0 is the initial heating rate in W/kg, μ and t are half-decay time and time, respectively.

For the viscous dissipation, which can be defined as:

$$H_D = \zeta \tau : \dot{\epsilon}^v \tag{6}$$

Where ζ is the heat conversion efficiency, and it depends on whether other deformational mechanisms are adopted (Thielmann & Kaus, 2012). In this work, ζ is set to 1, meaning that we assume all dissipation heat is converted into heat (e.g., Schmalholz et al., 2018). τ is the deviatoric stress tensor, and $\dot{\epsilon}^v$ is the visco-plastic component of the deviatoric strain rate tensor.

3 Model Configuration

3.1 Initial Conditions

Temperature is one of the key factors controlling the rheological structures (e.g., Katayama, 2021). We assume that the thermal profile of the research domain only composed of the crust and lithosphere-mantle, is determined by the 1-D steady conduction heat equation with radiogenic heat production, which is given by:

$$\frac{d}{dr}(r^2 k_x \frac{dT}{dr}) = -r^2 H_x \tag{7}$$

Where r is radius, or $r = R_p - z$, with R_p the planetary radius and z the depth. k is the thermal conductivity, and H is the internal heating source, which only consists of radiogenic heating source. x is the index representing different layers (i.e., the crust and lithosphere-mantle).

In order to obtain the boundary conditions (e.g., boundary temperature, layer thickness) that used to solve this equation, we carry out a one-dimensional parametric global evolution model of Mercury following our previous work (Xie et al., 2022). As discussed earlier, the recent study on the relationships between the crustal thickness and the mantle melting production suggested a thin crust with the thickness of 19±3km beneath the NSP, reflecting a low-degree mantle melting scenario (Beuthe et al., 2020). Therefore, the thickness of the crust can be used as a criterion to determine whether the outputs of the 1-D model are reasonable. Additionally, studies on the timing of the shortening tectonic features suggested that most thrust-faulting underway at 3.7±0.2Ga before present (b.p) (e.g., Giacomini et al., 2015, 2020; Crane & Klimczak, 2017). Hence, we adopt the results from the 1-D model at 3.8Ga b.p as for solving the initial temperature profile. In the end, after the model running done, we obtain a thin crust and a lithosphere-mantle with the thickness of around 19.1km and 110.8km, respectively. The computed initial temperature profile is integrated into the schematic diagram of the geometry (see below in Fig 2), where the temperature at the crust-mantle boundary (T_{CrMB}) and the bottom of the lithosphere-mantle (T_b) are about 754K and 1435K respectively. In addition, the corresponding output radiogenic heat production rate (RHPR) are about 9.37×10^{-11}W/kg and 9.37×10^{-12}W/kg. The value of the crustal RHPR is in line with the RHPR against time calculated with the Gamma-Ray Spectrometer measured data (e.g., Peplowski et al., 2011). Lastly, as required by the 2-D simulation, we set the reference temperature to be approximate to the temperature at crust-mantle boundary (T_{CrMB}). The output of the 1-D model can be found in Appendix B, and the data of temperature saved in .txt format can be accessed through the link provided by Open Research section.

The second key point is about the background bulk strain rate (hereinafter referred to as strain rate), which can impose significant impacts on the rheological structures of the lithosphere (e.g., Katayama, 2021). As for Mercury, a favored value by strength models is $10^{-17}s^{-1}$ (e.g., ductile-strength model in Zuber et al. (2010); Egea-González et al. (2012)). However, recent study on the stratigraphic relationships of thrust fault related features with craters limited the strain rate at the onset of faulting to an order of $10^{-20} \sim 10^{-21}s^{-1}$ (Crane & Klimczak, 2017). If the elastic properties of the rock are taken into account, then the strain rate during the lithospheric elastic deformation processes is probably between the order of 10^{-19} and $10^{-20}s^{-1}$ (Klimczak, 2015). In other words, in either case, the strain rate is much smaller than the commonly used in previous studies, although the actual value of strain rate may much larger when lithosphere breaks. Finally, combined with the arguments of the first point, we set the strain rate to $4.1\pm1.6\times10^{-20}s^{-1}$, which is the derived average value during the Calorian (i.e., one of the five time-stratigraphic systems of Mercury, 3.9∼3.5 to 3Ga b.p.) (Crane & Klimczak, 2017).

The basic parameters are given in Table 1.

3.2 Rheology

Regarding the rheology of Mercury's lithosphere (i.e., crust plus lithosphere-mantle). Considering the fact that no plate motions have been found on the surface of Mercury at present time, it is common to apply rheological laws such as power law (e.g., the dislocation creep) to characterize the rheology of Mercury's silicate shell (e.g., Egea-González et al., 2012; Thiriet et al., 2019). Using this type of rheology law can facilitate the planet's outer silicate shell becoming strong in a short period of time, which helps produce a large viscosity contrast between the planetary surface and the interior, resulting in a complete global plate or stagnant lid (Stern et al., 2018; Tosi & Padovan, 2021). But, should other creep laws be introduced?

Laboratory studies demonstrate that the temperatures, pressure and strain rates are the main factors controlling the rheology of rocky planets (e.g., Karato & Wu, 1993; Mei et al., 2010; Burov, 2011). Experiments on rocks under certain temperature and strain

Table 1. Basic Parameters

Symbols	Ref./Description	Values	Units
R_p	[1]Planetary radius	2440	km
R	[1]Gas constant	8.3144	$J \cdot mol^{-1} \cdot K^{-1}$
g	[1]Surface gravitational acceleration	3.7	m/s^2
α	[1]Thermal expansion coefficient	2×10^{-5}	K^{-1}
T_s	[1]Surface temperature	440	K
η_0	[2]Reference viscosity	1×10^{21}	$Pa \cdot s$
$\dot{\epsilon}_b$	[3]Background bulk strain rate	4.1×10^{-20}	s^{-1}
Q^0_{crust}	[4]Initial crustal heating rate	9.37×10^{-11}	W/kg
Q^0_{mantle}	[4]Initial mantle heating rate	9.37×10^{-12}	W/kg
T_{ref}	[4]Reference temperature	750	K

Ref.:1.Knibbe and van Westrenen (2018); 2.Thiriet et al. (2019)
Ref.:3.Crane and Klimczak (2019); 4.:Xie et al. (2022)

rates conditions suggest that for lower temperatures (approximately lower than 800K) and high strain rate, restrictions to glide of dislocations limits rates of straining, the deformation processes abide by Peierls creep, while for higher temperatures region, diffusion creep and power-law play the key role due to their strong sensitivity of temperature and strain rate (Kameyama et al., 1999; Mei et al., 2010; Molnar, 2020; Pleus et al., 2020). According to the initial conditions we discussed in previous section, the computed temperature profile supports the involvement of laws like Peierls creep in both the crust and part of the lithosphere-mantle. On the other hand, the deformation type indicates that most thrust-faults features found in NSP are interpreted as thin-rooted, rooting in a weak layer and propagating upward (e.g., Crane & Klimczak, 2019). Taking into account the low strain rate, we tend to reduce the overall strength of the lithosphere to ensure the existence of weak layer, and the Peierls creep have been proven to effectively reduce the overall strength of the lithosphere (e.g., Auzemery et al., 2020). In short, we conclude that it is reasonable and necessary to introduce the Peierls creep into our work. Finally, we apply a composite rheological model that combine Peierls, diffusion and dislocation creep to the research domain, assuming the viscosity as the pseudo-harmonic average of those three rheologies under isotropic applied stress (e.g., O'Neill & Zhang, 2019). The Peierls creep is given by (e.g., McCarthy et al., 2020):

$$\eta_{pei} = \frac{\gamma\sigma p}{2(A(\gamma\sigma_p)^n)^{1/(s+n)}} exp(\frac{H}{RT} \cdot \frac{(1-\gamma^p)^q}{s+n})\dot{\epsilon}_{II}^{\frac{1}{s+n}-1} \tag{8}$$

with

$$s = (\frac{H}{RT})pq(1-\gamma^p)^{q-1}\gamma^p \tag{9}$$

Where γ is the fitting parameters, σ_p is the Peierls stress, A is the pre-factor, and n is the stress exponent. p and q are the Peierls glide parameters, whereas the parameters depend on the geometry of obstacles that limit the dislocation motion and theoretical considerations suggest that $0 \leq p \leq 1$ and $1 \leq q \leq 2$ (Chowdhury et al., 2017; Jain et al., 2017). $\dot{\epsilon}$ is the effective strain rate, and $H = E + PV$, where E is the activation energy, V is the activation volume, R is the universal gas constant. P and T are pressure and temperature, respectively.

The generic form of dislocation creep law and diffusion creep law can be expressed as (e.g., Billen & Hirth, 2007):

$$\eta = fA^{\frac{-1}{n}}d^{\frac{m_1}{n}}(\dot{\epsilon}^v_{II})^{\frac{1-n}{n}}exp(\frac{E+PV}{nRT}) \tag{10}$$

Where f is a scaling factor that used to decrease the effective viscosity relative to the viscosity resulting from rock deformation experiments. A is the pre-factor, n is the power-law stress component, d is the grain size, m_1 is the grain size exponent, and $\dot{\epsilon}^v_{II}$ is the second invariant of the visco-plastic part of deviatoric stress tensor. E, P and V are the same as defined above. For diffusion creep, $n = 1$, $m_1 \neq 0$, and for dislocation creep, $n > 1, m_1 = 0$.

Finally, the viscosity can be expressed by (e.g., O'Neill & Zhang, 2019):

$$\eta = (\sum_i \eta_i^{-1})^{-1} \tag{11}$$

Where i is the index for different rheological laws.

Meanwhile, we utilize the Drcuker-Prager criterion (DP) to limit all the materials that undergo frictional/plastic deformation, which is also regarded as the extended Mohr-Coulomb criteria (Jiang & Xie, 2011; Alejano & Bobet, 2015). It has the following form:

$$\tau_d = C_0 \cdot cos(\phi) + P \cdot sin(\phi) \tag{12}$$

Where τ_d is the yield stress of DP, C_0 is the cohesion, ϕ is the internal friction angle, and P is the pressure.

In case of yielding, the effective viscosity is iteratively reduced until the corresponding stress equals the yield stress, that is:

$$\begin{cases} \eta_{eff} = \eta & \tau < \tau_d \\ \eta_{eff} = \frac{\tau_d}{2\tau_{II}} & \tau > \tau_d \end{cases} \tag{13}$$

Where τ_{eff} is the effective viscosity.

3.3 Lithology

In addition to the rheology, lithology is another key variable determining the strength of plastic deformation, because the plastic strength is generally controlled by the weakest constituent mineral in rocks (e.g., Azuma et al., 2014; Katayama, 2021). Recent geochemical works constrained the major surface potential mineralogy of Mercury to plagioclase, pyroxene and olivine. Particularly, in the NSP, it is plagioclase dominated (e.g., Namur & Charlier, 2017; Kaaden et al., 2017). As for the composition of the lithosphere-mantle of Mercury, an olivine-rich mantle is suggested and favored (Namur et al., 2016; Beuthe et al., 2020). Accordingly, we assume that a dried Olivine enriched lithosphere-mantle is covered by a dried Columbia Diabase (mainly composed of plagioclase) enriched crust (Kay & Dombard, 2019; Katayama, 2021), although the precise components of Mercury's interior are still unknown. Lastly, due to the lack of experiments on the Peierls and diffusion creep of Maryland/Columbia diabase, we replace the diffusion creep of diabase by plagioclase and apply a same Peierls creep of dry olivine indiscriminately to the crust and lithosphere-mantle (Mei et al., 2010; Katayama, 2021).

The parameters of rheology and lithology (conventionally named compositional fields in ASPECT) are given in Table 2 and 3.

3.4 Geometry setting

Given the initial temperature profile, strain rate and rheological laws, we can calculate the strength profile of the lithosphere using the parameters given in Table 1 to 3. The computed strength profile is used to subdivide the geometry of the research domain. We also introduce the Goetze criterion (Goetze & Evans, 1979) and Byerlee intermediate-high pressure law (hereinafter referred to as Byerlee law, referring to Klimczak (2015)), which are given by:

$$\tau_g = \frac{1}{2}(\rho g z - P_p) \tag{14}$$

Where τ_g is the shear stress of Goetze criterion in MPa, ρ is the density, g is the surface gravitational acceleration and z is the depth. P_p is the pore pressure, which is ignored in this work.

Table 2. Constant Parameters for Compositional fields

Symbols	Ref./Description	Crust	Lithosphere-mantle	Units
k	[1]Thermal conductivity	1.5	3.5	$W \cdot m^{-1} \cdot K^{-1}$
c	[1]Specific heat capacity	1000	11212	$J \cdot kg^{-1} \cdot K^{-1}$
ρ	[2]Average density	2950	3200	kg/m^3
C_0	[3]Cohesions	66	66	MPa
μ	[4]Elastic shear modulus	65	140	GPa
ϕ	[*]Internal friction angle	$30, 28$	$28, 30$	$degree$

Ref.:1.Knibbe and van Westrenen (2018); 2.Beuthe et al. (2020)
Ref.:3.Klimczak (2015); 4.Kay and Dombard (2019)
Ref.:*.Partially refer to Klimczak (2015)

Table 3. Distinct Parameters for Compositional fields

Symbols	Description	Crust	Lithosphere-mantle	Units
	[1]Dislocation creep			
E	Activation energy	485	535	kJ/mol
V	Activation volume	-	-	m^3/mol
A	Pre-factor	1.2×10^{-26}	4.85×10^{-17}	$Pa^{-n}s^{-1}$
n	Stress component	4.7	3.5	-
f	Scaling factor	1/2	1/2	-
	[2]Diffusion creep			
E	Activation energy	467	375	kJ/mol
V	Activation volume	-	8.2×10^{-6}	m^3/mol
A	Pre-factor	1.0×10^{-12}	1.5×10^{-15}	$m^{m_1}(Pa \cdot s^{-1})$
d	Grain size	2.0×10^{-3}	2.0×10^{-3}	m
m_1	Grain size exponent	3	3	-
n	Stress component	1	1	-
f	Scaling factor	1/2	1/2	-
	[3]Peierls creep			
H	Activation energy	320	320	kJ/mol
A	Pre-factor	1.4×10^{-9}	1.4×10^{-9}	$Pa^{-n}s^{-1}$
δ_p	Peierls stress	5.9×10^9	5.9×10^9	Pa
n	Stress component	2	2	-
p	Glide parameter p	0.5	0.5	-
q	Glide parameter q	1	1	-
γ	Scaling factor	0.17	0.17	-

Ref.:1.[Crameri and Kaus (2010); Katayama (2021)]
Ref.:2.[Crameri and Kaus (2010); Schulz et al. (2019)]
Ref.:3.[Mei et al. (2010)]

And

$$\begin{cases} \eta_b = 2\rho gz & \rho gz < 110MPa \\ \eta_b = \frac{1}{2}(2.1\rho gz + 210) & \rho gz > 110MPa \end{cases} \tag{15}$$

Where τ_b is the shear stress of Byerlee law in MPa, and the rest of parameters are defined above.

The reasons why the Goetze criterion and Byerlee law are introduced as follows. First of all, laboratory studies suggest that there can be three types of rock deformation under lithospheric conditions, i.e., brittle, semi-brittle and viscous deformation (D. Kohlstedt et al., 1995; Mei et al., 2010). Although the dynamic mechanism of semi-brittle deformation is poorly understood, we assume that once the brittle strength is approximately equal to one-fifth of the plastic strength, then the transition from brittle to semi-brittle deformation will be initiated (e.g., D. Kohlstedt et al., 1995; D. L. Kohlstedt & Mackwell, 2009). In practice, the Goetze criterion is used to indicate the transition between semi-brittle and viscous deformation (e.g., D. L. Kohlstedt & Mackwell, 2009; Mei et al., 2010; Zhong & Watts, 2013; Bellas et al., 2020). So far, we can use the computed values of the brittle, plastic strength of the lithosphere and Goetze criterion as the basis for subdividing the structure of lithosphere (see below). Secondly, the Drucker-Prager criterion can be regarded as the generalization form of Mohr-Coulomb criteria but has a more stable performance in high-dimensional numerical simulations. However, the pressure in Eq.(12) is the total pressure rather than the lithostatic pressure P_l (i.e., under compression conditions: $P_l = \rho gz$). Multiple works have been devoted to revealing the relationship between the total and lithostatic pressure (e.g., Gerya, 2015; Marques et al., 2018; Zuza et al., 2020). A rough estimate is that when the internal friction angle (ϕ) is 30°, the total pressure is about twice as large as lithostatic pressure under compression conditions (Zuza et al., 2020). Therefore, the Eq.(12) can be recast as:

$$\tau_d \approx C_0 \cdot cos(\phi) + 2\rho gz \cdot sin(\phi) \tag{16}$$

As another commonly used formula for calculating the brittle strength of the lithosphere (D. L. Kohlstedt & Mackwell, 2009), the additionally introduced Byerlee law (i.e., Eq.(15)) is used to compare the result calculated by Eq.(16).

Fig 1 illustrates the shear stress profile of the crust and lithosphere-mantle at the strain of $4.1{\times}10^{-20}s^{-1}$, which is computed via $\tau = 2\eta\dot{\epsilon}$, where $\dot{\epsilon}$ is the effective strain rate, η is the viscosity given by Eq.(11). Fig 1.A depicts the shear stress profile of the crust, where CD20 represents the shear strength of Columbia Diabase. Correspondingly, CD20/5 represents the one-fifth of CD20.

It can be seen that,

1. the brittle strength computed by Drucker-Prager criterion (DP) starts from the point O and intersects with CD20/5 at point A (the corresponding depth is about 8.5km), which indicates that deformation type in segment OA is brittle, while deformation changes to semi-brittle deformation from point A.
2. the Goetze criterion and CD20 have no intersection, suggesting that there is no transition from semi-brittle to viscous deformation in the crust.

Therefore, the crust can be subdivided into two parts: the upper crust that undergoes brittle deformation (segment OA) and the semi-brittle region (segment AB).

Similarly, Fig1.B shows the shear stress profile in the lithosphere-mantle. OL20 represents the shear strength of Olivine, and OL20/5 is one-fifth of that. It is obviously to find out that OL/20 is always smaller than DP in the lithosphere-mantle, while OL and Goetze criterion intersects at point C (the corresponding depth is about 30.85km). Combing the results from Fig1.A, we conclude that the semi-brittle deformation region from point A extends to point C, after that, the viscous deformation dominates. Hence, we can treat the lithosphere-mantle as being made of two parts: the semi-brittle region and mantle.

The results calculated by Eq.(15) and Eq.(16) show that the difference between them is not large. Considering that the total pressure may be more than twice of the litho-

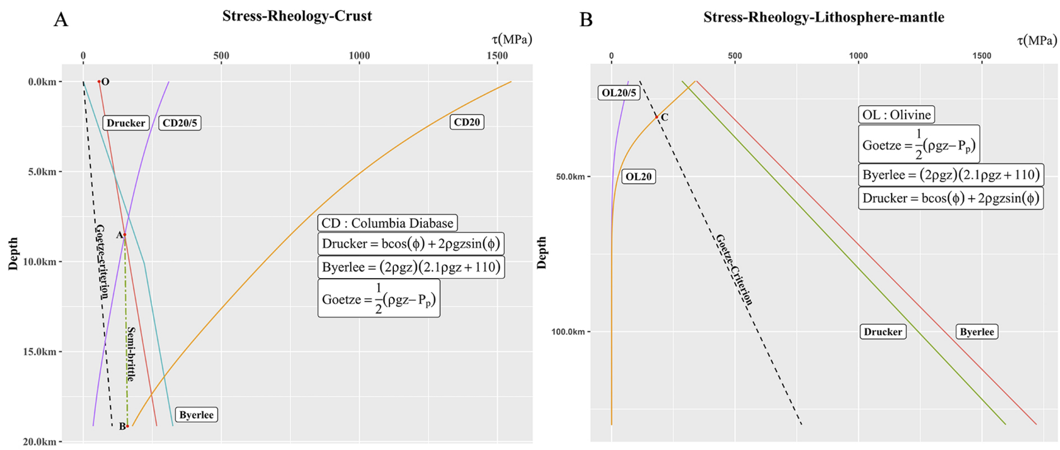

Figure 1. The shear stress profile in the crust and lithosphere-mantle at the strain rate of 4.1e-20s^{-1}. In both subplots, the horizontal axis represents the shear stress in MPa, the vertical axis represents the depth in km, which stands for 1000 meters. A) In the crust, CD represents the shear strength of Columbia Diabase, and CD/5 is one-fifth of that. B) In the lithosphere-mantle, OL represents the shear strength of Olivine, and OL/5 is one-fifth of that.

static pressure (e.g., Gerya, 2015), the use of Eq.(16) is reasonable and acceptable. It is worth noting that Eq.(16) is only used to divide the geometry model at the initial configuration of the simulation, while in the subsequent numerical simulations, we still use Eq.(12) instead.

In summary, the research domain is subdivided into four parts, from shallow to deep: the upper crust (z: 0-8.5km), the semi-brittle region of the crust (z: 8.5-19.1km), the semi-brittle region of the lithosphere-mantle (z: 19.1-30.85km) and mantle (z: 30.85-130km) (refer to Fig 2). Although it is difficult to accurately capture the processes of semi-brittle deformation in numerical simulations, we can still approximate its effects with a smaller internal friction coefficient, i.e., a smaller internal friction angle (e.g., Pleus et al., 2020). As a result, the research domain was originally composed of only the homogenous crust and lithosphere-mantle, but now there are four mechanical discontinuous structures.

3.5 Geometry configuration

Regarding the model configuration, a Cartesian geometry with dimensions of 800×130km is applied, where 130km is the sum of the thickness of the crust and lithosphere-mantle. The mesh of our geometry has a resolution of 125×125m above the depth of 60km and 250×250m below. Studies on the inversion of gravity anomalies revealed the relationship between the surface topography and the lateral heterogeneous in the crust-mantle interface (e.g., James et al., 2015; Beuthe et al., 2020). Therefore, as an extreme case where thrust-faults are generated from the bottom of the crust (e.g., Beuthe et al., 2020; Peterson et al., 2020), we set up topography (indicator: point U, see Fig 2) at the CrMB, which can help break the symmetry of the model and promote strain localization. This model is heated from the bottom and cooled from the top, while the left and right boundaries are insulated. The top and the bottom boundary are free surface and free slip, respectively. A constant strain rate of $4.1 \times 10^{-20} s^{-1}$ is generated by the horizontal velocity applied on the two lateral boundaries. Fig 2 gives the disproportionate schematic diagram of the geometry model.

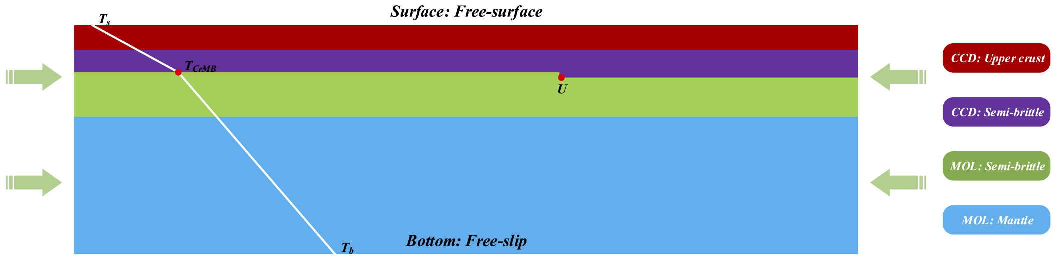

Figure 2. The schematic diagram of the geometry model with dimensions of 800×130km, where the surface temperature (T_s) is 440K, the temperature at the crust-mantle boundary (T_{CrMB}) is 754K and the bottom temperature (T_b) is 1435K. The geometry is composed of a dried Columbia Diabase enriched crust and olivine enriched lithosphere-mantle. The research domain is vertically subdivided into four layers: the upper crust (z: 0-8.5km) and the crustal semi-brittle region (z: 8.5-19.1km), lithosphere-mantle semi-brittle region (z: 19.1-30.85km) and mantle (z: 30.85-130km). We set up topography (point U as an indicator, its corresponding x-coordinate is 480km) at the crust-mantle boundary of 1.5km, which can help break the symmetry of the model and initiate the convection. This model is heated from the bottom and cooled from the top, while the left and right boundaries are insulated. The top and the bottom boundary are free surface and free slip, respectively. A constant background bulk strain rate is generated by the horizontal velocity applied on the two lateral boundaries. CCD: Crustal Columbia Diabase. MOL: Mantle Olivine.

4 Results

Our two-dimensional numerical simulation starts at 3.8Ga b.p and lasts for 70Myr. Fig 3 depicts the square root of the second invariant of the shear strain rate tensor (hereinafter referred to as SRI, used as the effective strain rate, $\tau_{II} = \sqrt{\tau_{11}^2 + \tau_{12}^2}$, referring to Gerya (2019)) at 10Myr, 40Myr and 70Myr with the topography at CrMB of 1.5km (see Fig 2). First of all, it can be seen that the high-SRI regions are mainly concentrated in the semi-brittle region of the crust, which has an average depth of 10km, and their distribution patterns are related to the distance from the topography indicator at CrMB (i.e., point U). Depending on the distance from point U, from left to right, we divide the crustal geometry into three sections, i.e., section H, section T (framed by black line) and section F.

Among them, neither the value of high-SRI nor the distribution pattern in section H has changed much over time, which provides a stable and concentrated high-SRI region within the crust at a shallow depth. While the strain status in section T is the most complicated, strain localizes in the section T due to the closest proximity to the topography at the CrMB. The high-SRI region penetrates almost the entire curst and gradually concentrates near the surface along with time. As to the section F, although the distribution pattern of high-SRI regions is similar to that in section H, its value of SRI is lower and distributed in a scatter area. More notably, the high-SRI region in the section F is the most sensitive to time. It is easy to figure out that when the time is 70Myr, there are almost no high-SRI region in section F, and it moves down to the lithosphere-mantle instead.

Apparently, the strain status within the lithosphere is directly reflected in the surface topography. Therefore, we further calculate the corresponding surface topography, which are illustrated in Fig 4. In Fig 4, the black point U is used to indicate the relative position of the surface topography and the topography at the CrMB. The point L and A represents the lowest and highest surface relief, respectively. Their precise values are listed in Table 4.

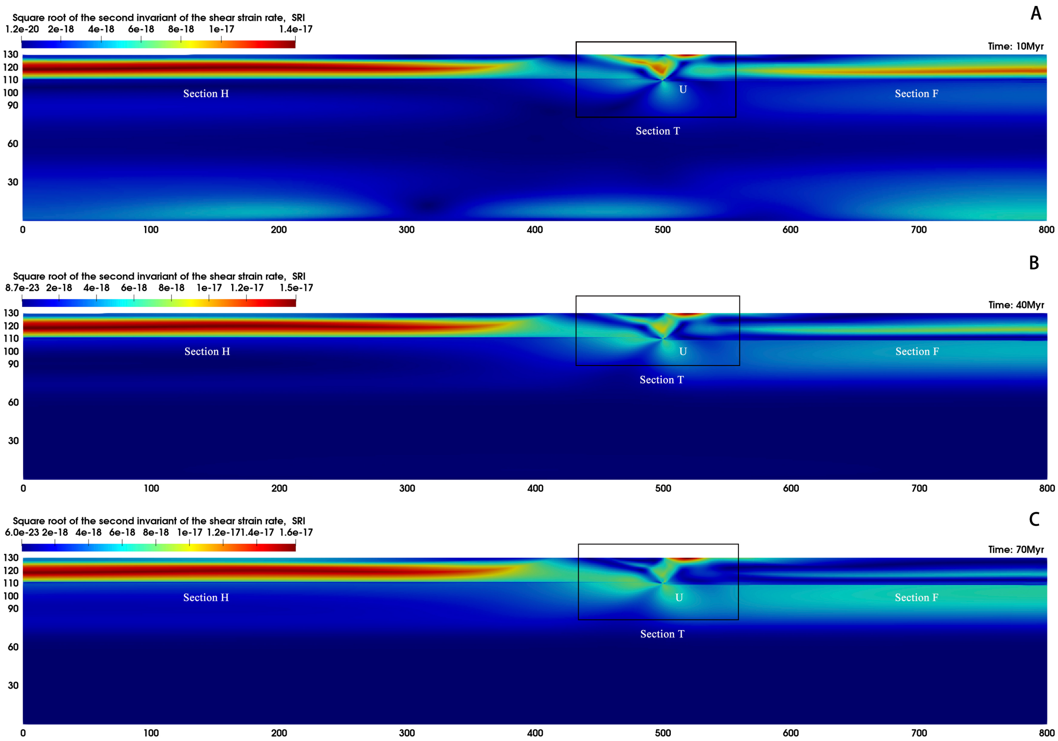

Figure 3. The snapshots of the square root of the second invariant of the shear strain rate (SRI) at A) 10Myr, B) 40Myr and C) 70Myr. The vertical axis represents the thickness (y) in km (the depth can be calculated by z=130-y, where z is depth), the horizontal axis represents the x-direction extension in km. The high SRI concentrated regions are divided into three sections, from left to right, which are section H, section T (framed by black line) and section F.

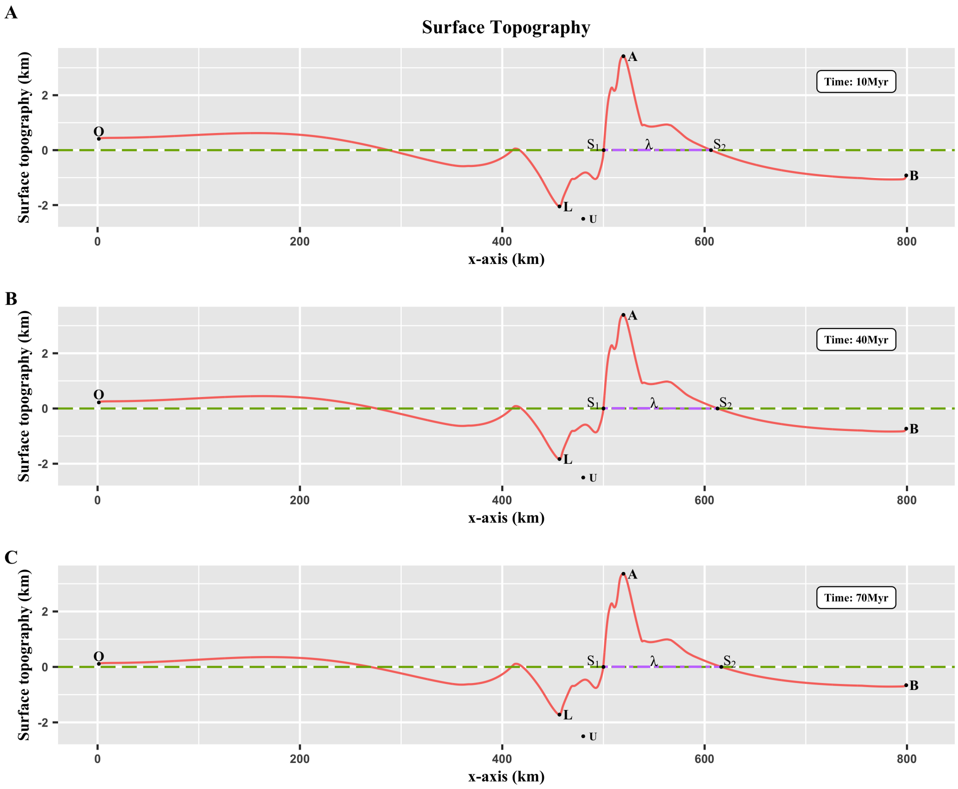

Figure 4. The surface topography (red line) at A) 10Myr, B) 40Myr and C) 70Myr with CrMB topography of 1.5km. The green dashed-line represents the horizon (i.e., depth = 0). The black point U represents the topography indicator at the CrMB (not the true burial depth in Fig 2 and 3), which is used to indicate the relative position of the surface topography and the topography at the CrMB. Point L and A indicates the lowest and highest surface topography.

Our simulation results in a characteristic positive relief surface topography. Referring to previous geological works (e.g., Byrne et al., 2018), we also define the line LS_1A in Fig 4 as the forelimb and the line AS_2B as the backlimb. It is clear to find out a steep forelimb and a gently sloping backlimb, which is well consistent with the characteristic geomorphic cross section of lobate scarps (e.g., Watters et al., 2009; Byrne et al., 2018; Klimczak et al., 2019). In addition, according to the data listed in Table 4, the surface topography gradually relaxes as the simulation time increases. That is, particularly, the summit (point A) is falling and the lowest point L is approaching the surface. At the same time, the rate of topographic relaxation is decreasing over time. The reason for this result lies in the fading away of high-SRI regions in section T and F, and the stability of the high-SRI region near the surface in section T ensures that the surface topography has not changed radically along with time.

5 Discussion

So far, this work has created a high strain rate region within the lithosphere at a shallow depth and obtained a well consistent surface topography of typical shortening features discovered in the NSP at the present (Crane & Klimczak, 2019; Peterson et al., 2020). Nevertheless, it is worthy of noting that the starting point of this work is to pro-

Table 4. The precise value of surface topographical indicators over time

Symbols	10Myr	40Myr	70Myr	Units
O	0.7137	0.2297	0.1146	km
L	-2.0503	-1.8365	-1.7212	km
A	3.4208	3.3902	3.3654	km
B	-0.9239	-0.7346	-0.6679	km
λ	106	112.75	116.6	km

pose a lithospheric mechanical model that satisfies the assumption of fragile layer within the lithosphere assumed by thin-rooted deformation, to the study the formation of thrust-faults related landforms, although we cannot confirm whether the fragile layer exists, or its thickness, composition and converge are still poorly understood (e.g., Crane & Klimczak, 2019). We verify the plausibility of this model by means of numerical simulations, from the results, our model works.

However, for numerical simulation, it is sensitive to the input parameters. In addition to the parameters we argued in previous section (e.g., temperature, rheological parameters), the surface topography is also attribute to the topography at the CrMB. For comparsion, we also calculate the surface topography when the topography at the CrMB is 1km, and the result can be found in the Supporting Information. It can be seen that the computed surface relief is gentler and its pattern is more complex. Recently, Crane and Klimczak (2019) analyzed and mapped the detailed map of tectonic patterns of shortening features in NSP, their work highlighted the complexity of the tectonic patterns of the geological landforms. Our simulations suggest that their conclusion can be related to the topography in the lithosphere. Although the tectonic patterns are controlled by many factors, our work emphasizes the importance and sensitivity of the relationship between the surface topography and the relief at the CrMB, which deserves further research in numerical simulations.

Additionally, since this paper simulates the thermo-dynamic process of 3.8 billion years ago, taking into account the observed tendency of the relaxation of the terrain (refer to Table 4) as well as the subsequent geological activities, the obtained surface relief will be closer to what MESSENGER imaged. A significant feature of the NSP is the continuous volcanic activity compared to other regions in Mercury (e.g., Thomas & Rothery, 2019). Researches on the crater size-frequency distributions implies that large-volume volcanism on Mercury had ceased around 3.5Ga b.p, younger than the underlying craters and the most shortening features in smooth plains (e.g., Byrne et al., 2016; Thomas & Rothery, 2019). Moreover, modeling of temporal degradation of crater shape topography constraints the lava flow thickness within the NSP to several hundred meters to kilometers (Head et al., 2011; Ostrach et al., 2015; Du et al., 2020). Therefore, the influence of volcanism on the formation, distribution and orientation of thrust-faults related landforms in the NSP is also worthy of further investigation.

6 Conclusion

In this paper, we propose a thermo-dynamic model from the perspective of temperature, rheological laws and strain rate, to study the formation of the thrust-faults related landforms in the northern smooth plains of Mercury under low strain rate via 2-D viscoelastic-plastic numerical simulations. Mechanically, our model subdivides the lithosphere into several mechanical discontinuous layers by introducing the semi-brittle deformation, which provides a transition zone between the brittle and viscous deformation region, refining the commonly used strength model of Mercury's lithosphere (Zuber et al., 2010; Egea-González et al., 2012). This simulation results in a stable and concentrated high strain rate region in the crust and geomorphic consistent surface topography with typical thrust-faults related landforms found in the northern smooth plains of Mercury. Future studies can be extended to higher-dimensional on this basis to study the distribution, orientation and other characteristics of the thrust-faults related landforms on Mercury.

Acknowledgments
This work is supported by National Natural Science Foundation of China under award 11973072, 12173068 and 11773058. We also thank the Computational Infrastructure for Geodynamics (geodynamics.org) which is funded by the National Science Foundation under award EAR-0949446 and EAR-1550901 for supporting the development of ASPECT.

7 Open Research

The codes that reproduce the outputs of the two-dimensional numerical simulations are available on Zenodo (`https://doi.org/10.5281/zenodo.5912132`).

Appendix A

For the constitutive equation (Eq.(1)), $\bar{\tau}$ is the Jaumann corotational stress rate tensor, which is defined as (e.g., Patočka et al., 2017):

$$\bar{\tau} = \dot{\tau} + \tau w - w\tau = \frac{\partial \tau}{\partial t} + \tau w - w\tau \tag{A1}$$

Where w is the spin tensor, which follows:

$$w_{ij} = \frac{1}{2}(\nabla u - \nabla u^T) = \frac{1}{2}(\frac{\partial u_j}{\partial x_i} - \frac{\partial u_i}{\partial x_j}) \tag{A2}$$

We refer to Moresi et al. (2003) to express the Jaumann corotational stress rate in a difference form in order to obtain a stress-strain rate relation. Defining the current time as t, and a material timescale as Δt_m, the Eq.(A.1) can be rewritten as:

$$\bar{\tau}^{t+\Delta t_m} \approx \frac{\tau^{t+\Delta t_m} - \tau^t}{\Delta t_m} - w^t\tau^t + \tau^t w^t \tag{A3}$$

Introducing the Maxwell relaxation time $\Theta = \frac{\tau}{\eta}$, integrating this term into Eq.(A.3), we have:

$$\tau^{t+\Delta t_m} = \frac{2\eta\Delta t_m}{\Theta + \Delta t_m}\hat{D}^{t+\Delta t_m} + \frac{\Theta}{\Theta + \Delta t_m}\tau^t + \frac{\Theta\Delta t_m}{\Delta t_m + \Theta}(w^t\tau^t - \tau^t w^t) \tag{A4}$$

Let the effective viscosity be:

$$\eta_{eff} = \eta\frac{\Delta t_m}{\Delta t_m + \Theta} \tag{A5}$$

then rewrite the Eq.(A.4) as:

$$\tau^{t+\Delta t_m} = \eta_{eff}(2\hat{D}^{t+\Delta t_m} + \frac{\tau^t}{\mu\Delta t_m} + \frac{w^t\tau^t - \tau^t w^t}{\mu}) \tag{A6}$$

Where the elastic force term is:

$$F_i^{e,t} = -\frac{\eta_{eff}}{\mu\Delta t^e}\nabla\cdot\tau_{ij}^t \tag{A7}$$

Adding the elastic force term to the equation of momentum, we finally obtain:

$$\tau_{ij,j}^{t+\Delta t^e} - \Delta P + f_i + F_i^{e,t} = 0 \tag{A8}$$

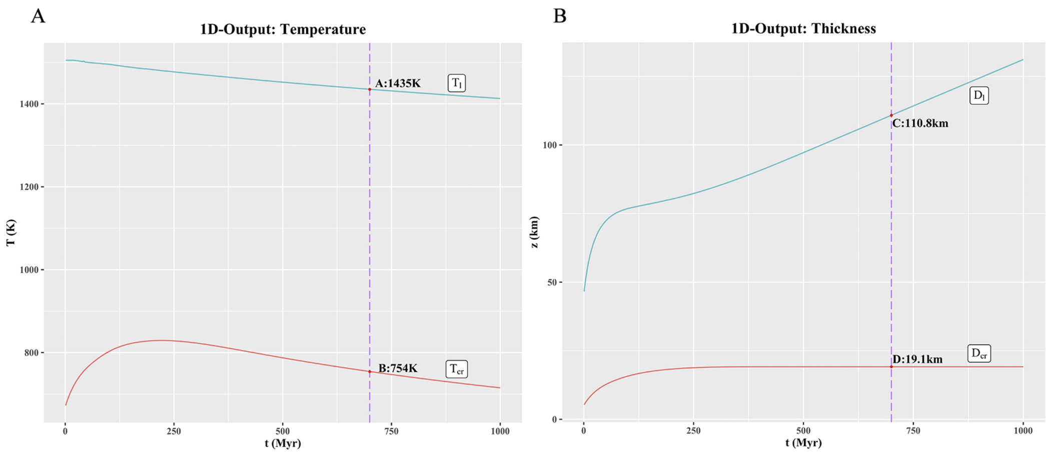

Figure B1. Output of the 1-D global parametric model of Mercury. In order to better display the results, we only show the results of the first 1 billion years. In both subplots, the purple vertical line indicates the time at 700 million years, and its intersections with other four curves (i.e., A, B, C and D) are used to calculate the initial temperature profile. A). The temperature at the bottom of the crust (T_{cr}) and lithosphere-mantle (T_l) over time during the first 1 billion years. B). The thickness of the crust (D_{cr}) and lithosphere-mantle (D_l) over time during the first 1 billion years.

Appendix B

The 1-D global parametric evolution model of Mercury, which refers to Xie et al. (2022), is used to compute the boundary conditions required for the initial temperature profile. The shown results include the temperature at the bottom of the crust (T_{cr}), lithosphere-mantle (T_l), and the thickness of the crust (D_{cr}) and lithosphere-mantle (D_l). The values of radioactive heating rate in the lithosphere can be found in previous section.

References

Alejano, L. R., & Bobet, A. (2015). Drucker–prager criterion. In R. Ulusay (Ed.), *The isrm suggested methods for rock characterization, testing and monitoring: 2007-2014* (pp. 247–252). Cham: Springer International Publishing. Retrieved from `https://doi.org/10.1007/978-3-319-07713-0_22` doi: 10.1007/978-3-319-07713-0_22

Auzemery, A., Willingshofer, E., Yamato, P., Duretz, T., & Sokoutis, D. (2020). Strain localization mechanisms for subduction initiation at passive margins. *Global and Planetary Change*, *195*, 103323.

Azuma, S., Katayama, I., & Nakakuki, T. (2014). Rheological decoupling at the moho and implication to venusian tectonics. *Scientific Reports*, *4*.

Banks, M. E., Xiao, Z., Watters, T. R., Strom, R. G., Braden, S. E., Chapman, C. R., . . . Byrne, P. K. (2015). Duration of activity on lobate-scarp thrust faults on mercury. *Journal of Geophysical Research: Planets*, *120*(11), 1751–1762.

Bellas, A., Zhong, S., & Watts, A. (2020). Constraints on the rheology of the lithosphere from flexure of the pacific plate at the hawaiian islands. *Geochemistry, Geophysics, Geosystems*, *21*(2), e2019GC008819.

Beuthe, M., Charlier, B., Namur, O., Rivoldini, A., & Van Hoolst, T. (2020). Mercury's crustal thickness correlates with lateral variations in mantle melt production. *Geophysical Research Letters*, *47*(9), e2020GL087261.

Billen, M. I., & Hirth, G. (2007). Rheologic controls on slab dynamics. *Geochemistry, Geophysics, Geosystems*, *8*(8).

Burov, E. B. (2011). Rheology and strength of the lithosphere. *Marine and Petroleum Geology*, *28*(8), 1402–1443.

Byrne, P. K., Klimczak, C., & Şengör, A. (2018). The tectonic character of mercury. *Mercury. The View after MESSENGER. Edited by Sean C. Solomon*, 249–286.

Byrne, P. K., Klimczak, C., Şengör, A. C., Solomon, S. C., Watters, T. R., Hauck, S. A., et al. (2014). Mercury's global contraction much greater than earlier estimates. *Nature Geoscience*, *7*(4), 301–307.

Byrne, P. K., Ostrach, L. R., Fassett, C. I., Chapman, C. R., Denevi, B. W., Evans, A. J., . . . Solomon, S. C. (2016). Widespread effusive volcanism on mercury likely ended by about 3.5 ga. *Geophysical Research Letters*, *43*(14), 7408–7416.

Chowdhury, P., Gerya, T., & Chakraborty, S. (2017). Emergence of silicic continents as the lower crust peels off on a hot plate-tectonic earth. *Nature Geoscience*, *10*(9), 698–703.

Crameri, F., & Kaus, B. J. (2010). Parameters that control lithospheric-scale thermal localization on terrestrial planets. *Geophysical Research Letters*, *37*(9).

Crane, K. T., & Klimczak, C. (2017). Timing and rate of global contraction on mercury. *Geophysical Research Letters*, *44*(7), 3082–3089.

Crane, K. T., & Klimczak, C. (2019). Tectonic patterns of shortening landforms in mercury's northern smooth plains. *Icarus*, *317*, 66–80.

Denevi, B. W., Ernst, C. M., Meyer, H. M., Robinson, M. S., Murchie, S. L., Whitten, J. L., . . . others (2013). The distribution and origin of smooth plains on mercury. *Journal of Geophysical Research: Planets*, *118*(5), 891–907.

Du, J., Wieczorek, M. A., & Fa, W. (2020). Thickness of lava flows within the northern smooth plains on mercury as estimated by partially buried craters. *Geophysical Research Letters*, *47*(20), e2020GL090578.

Egea-González, I., Ruiz, J., Fernández, C., Williams, J.-P., Márquez, Á., & Lara, L. M. (2012). Depth of faulting and ancient heat flows in the kuiper region of mercury from lobate scarp topography. *Planetary and Space Science*, *60*(1), 193–198.

Gerya, T. (2015). Tectonic overpressure and underpressure in lithospheric tectonics and metamorphism. *Journal of Metamorphic Geology*, *33*(8), 785–800.

Gerya, T. (2019). *Introduction to numerical geodynamic modelling.* Cambridge University Press.

Giacomini, L., Massironi, M., Galluzzi, V., Ferrari, S., & Palumbo, P. (2020). Dating long thrust systems on mercury: New clues on the thermal evolution of the planet. *Geoscience Frontiers*, *11*(3), 855–870.

Giacomini, L., Massironi, M., Marchi, S., Fassett, C., Di Achille, G., & Cremonese, G. (2015). Age dating of an extensive thrust system on mercury: implications for the planet's thermal evolution. *Geological Society, London, Special Publications*, *401*(1), 291–311.

Goetze, C., & Evans, B. (1979). Stress and temperature in the bending lithosphere as constrained by experimental rock mechanics. *Geophysical Journal International*, *59*(3), 463–478.

Head, J. W., Chapman, C. R., Strom, R. G., Fassett, C. I., Denevi, B. W., Blewett, D. T., . . . others (2011). Flood volcanism in the northern high latitudes of mercury revealed by messenger. *Science*, *333*(6051), 1853–1856.

Heister, T., Dannberg, J., Gassmöller, R., & Bangerth, W. (2017). High accuracy mantle convection simulation through modern numerical methods–ii: realistic models and problems. *Geophysical Journal International*, *210*(2), 833–851.

Jain, C., Korenaga, J., & Karato, S.-i. (2017). On the yield strength of oceanic lithosphere. *Geophysical Research Letters*, *44*(19), 9716–9722.

James, P. B., Zuber, M. T., Phillips, R. J., & Solomon, S. C. (2015). Support of long-wavelength topography on mercury inferred from messenger measurements of gravity and topography. *Journal of Geophysical Research: Planets*, *120*(2), 287–310.

Jiang, H., & Xie, Y. (2011). A note on the mohr–coulomb and drucker–prager strength criteria. *Mechanics Research Communications*, *38*(4), 309–314.

Kaaden, K. E. V., McCubbin, F. M., Nittler, L. R., Peplowski, P. N., Weider, S. Z., Frank, E. A., & Mccoy, T. J. (2017). Geochemistry, mineralogy, and petrology of boninitic and komatiitic rocks on the mercurian surface: Insights into the mercurian mantle. *Icarus*, *285*, 155-168.

Kameyama, M., Yuen, D. A., & Karato, S.-I. (1999). Thermal-mechanical effects of low-temperature plasticity (the peierls mechanism) on the deformation of a viscoelastic shear zone. *Earth and Planetary Science Letters*, *168*(1-2), 159–172.

Karato, S.-i., & Wu, P. (1993). Rheology of the upper mantle: A synthesis. *Science*, *260*(5109), 771–778.

Katayama, I. (2021). Strength models of the terrestrial planets and implications for their lithospheric structure and evolution. *Progress in Earth and Planetary Science*, *8*(1), 1–17.

Kay, J. P., & Dombard, A. J. (2019). Long-wavelength topography on mercury is not from folding of the lithosphere. *Icarus*, *319*, 724–728.

Klimczak, C. (2015). Limits on the brittle strength of planetary lithospheres undergoing global contraction. *Journal of Geophysical Research: Planets*, *120*(12), 2135–2151.

Klimczak, C., Byrne, P. K., Şengör, A. C., & Solomon, S. C. (2019). Principles of structural geology on rocky planets. *Canadian Journal of Earth Sciences*, *56*(12), 1437–1457.

Knibbe, J. S., & van Westrenen, W. (2018). The thermal evolution of mercury's fe–si core. *Earth and Planetary Science Letters*, *482*, 147–159.

Kohlstedt, D., Evans, B., & Mackwell, S. (1995). Strength of the lithosphere: Constraints imposed by laboratory experiments. *Journal of Geophysical Research: Solid Earth*, *100*(B9), 17587–17602.

Kohlstedt, D. L., & Mackwell, S. J. (2009). Strength and deformation of planetary lithospheres. In T. R. Watters & R. A. Schultz (Eds.), *Planetary tectonics* (p. 397–456). Cambridge University Press. doi: 10.1017/CBO9780511691645.010

Kronbichler, M., Heister, T., & Bangerth, W. (2012). High accuracy mantle convection simulation through modern numerical methods. *Geophysical Journal International*, *191*(1), 12–29.

Marques, F., Ranalli, G., & Mandal, N. (2018). Tectonic overpressure at shallow depth in the lithosphere: The effects of boundary conditions. *Tectonophysics*, *746*, 702–715.

McCarthy, A., Tugend, J., Mohn, G., Candioti, L., Chelle-Michou, C., Arculus, R., . . . Müntener, O. (2020). A case of ampferer-type subduction and consequences for the alps and the pyrenees. *American Journal of Science*, *320*(4), 313–372.

Mei, S., Suzuki, A., Kohlstedt, D., Dixon, N., & Durham, W. (2010). Experimental constraints on the strength of the lithospheric mantle. *Journal of Geophysical Research: Solid Earth*, *115*(B8).

Michel, N. C., Hauck, S. A., Solomon, S. C., Phillips, R. J., Roberts, J. H., & Zuber, M. T. (2013). Thermal evolution of mercury as constrained by messenger observations. *Journal of Geophysical Research: Planets*, *118*(5), 1033–1044.

Molnar, P. (2020). The brittle-plastic transition, earthquakes, temperatures, and strain rates. *Journal of Geophysical Research: Solid Earth*, *125*(7), e2019JB019335.

Moresi, L., Dufour, F., & Mühlhaus, H.-B. (2003). A lagrangian integration point finite element method for large deformation modeling of viscoelastic geomaterials. *Journal of computational physics*, *184*(2), 476–497.

Namur, O., & Charlier, B. (2017). Silicate mineralogy at the surface of mercury. *Nature Geoscience*, *10*(1), 9–13.

Namur, O., Collinet, M., Charlier, B., Grove, T. L., Holtz, F., & McCammon, C. (2016). Melting processes and mantle sources of lavas on mercury. *Earth and Planetary Science Letters*, *439*, 117–128.

O'Neill, C., & Zhang, S. (2019). Chapter 4 - modeling early earth tectonics: The case for stagnant lid behavior. In M. J. Van Kranendonk, V. C. Bennett, & J. E. Hoffmann (Eds.), *Earth's oldest rocks (second edition)* (Second Edition ed., p. 65-80). Elsevier. Retrieved from `https://www.sciencedirect.com/science/article/pii/B9780444639011000046` doi: https://doi.org/10.1016/B978-0-444-63901-1.00004-6

Ostrach, L. R., Robinson, M. S., Whitten, J. L., Fassett, C. I., Strom, R. G., Head, J. W., & Solomon, S. C. (2015). Extent, age, and resurfacing history of the northern smooth plains on mercury from messenger observations. *Icarus*, *250*, 602–622.

Padovan, S., Wieczorek, M. A., Margot, J.-L., Tosi, N., & Solomon, S. C. (2015). Thickness of the crust of mercury from geoid-to-topography ratios. *Geophysical Research Letters*, *42*(4), 1029–1038.

Patočka, V., Čadek, O., Tackley, P. J., & Čížková, H. (2017). Stress memory effect in viscoelastic stagnant lid convection. *Geophysical Journal International*, *209*(3), 1462–1475.

Peplowski, P. N., Evans, L. G., Hauck, S. A., McCoy, T. J., Boynton, W. V., Gillis-Davis, J. J., ... others (2011). Radioactive elements on mercury's surface from messenger: Implications for the planet's formation and evolution. *science*, *333*(6051), 1850–1852.

Peterson, G. A., Johnson, C. L., Byrne, P. K., & Phillips, R. J. (2020). Fault structure and origin of compressional tectonic features within the smooth plains on mercury. *Journal of Geophysical Research: Planets*, *125*(7), e2019JE006183.

Pleus, A., Ito, G., Wessel, P., & Frazer, L. N. (2020). Rheology and thermal structure of the lithosphere beneath the hawaiian ridge inferred from gravity data and models of plate flexure. *Geophysical Journal International*, *222*, 207-224.

Schmalholz, S. M., & Duretz, T. (2015). Shear zone and nappe formation by thermal softening, related stress and temperature evolution, and application to the alps. *Journal of Metamorphic Geology*, *33*, 887-908.

Schmalholz, S. M., Duretz, T., Hetényi, G., & Medvedev, S. (2018). Distribution and magnitude of stress due to lateral variation of gravitational potential energy between indian lowland and tibetan plateau. *Geophysical Journal International*.

Schulz, F. T., Tosi, N., Plesa, A., & Breuer, D. (2019). Stagnant-lid convection with diffusion and dislocation creep rheology: Influence of a non-evolving grain size. *Geophysical Journal International*.

Solomon, S. C., Nittler, L. R., & Anderson, B. J. (2018). *Mercury: The view after messenger* (Vol. 21). Cambridge University Press.

Sori, M. M. (2018). A thin, dense crust for mercury. *Earth and Planetary Science Letters*, *489*, 92-99.

Stern, R. J., Gerya, T. V., & Tackley, P. J. (2018). Stagnant lid tectonics: Perspectives from silicate planets, dwarf planets, large moons, and large asteroids. *Geoscience frontiers*, *9*, 103-119.

Thielmann, M., & Kaus, B. J. P. (2012). Shear heating induced lithospheric-scale localization: Does it result in subduction? *Earth and Planetary Science Letters*, *359*, 1-13.

Thiriet, M., Breuer, D., Michaut, C., & Plesa, A. (2019). Scaling laws of convection for cooling planets in a stagnant lid regime. *Physics of the Earth and Planetary Interiors*.

Thomas, R. J., & Rothery, D. A. (2019, 02). Volcanism on Mercury. *Elements*, *15*(1), 27-32. Retrieved from https://doi.org/10.2138/gselements.15.1.27 doi: 10.2138/gselements.15.1.27

Tosi, N., & Padovan, S. (2021). Mercury, moon, mars. In *Mantle convection and surface expressions* (p. 455-489). American Geophysical Union (AGU). Retrieved from https://agupubs.onlinelibrary.wiley.com/doi/abs/10.1002/9781119528609.ch17 doi: https://doi.org/10.1002/9781119528609.ch17

Watters, T. R. (2021). A case for limited global contraction of mercury. *Communications Earth & Environment*, *2*.

Watters, T. R., James, P. B., & Selvans, M. M. (2021). Mercury's crustal thickness and contractional strain. *Geophysical Research Letters*.

Watters, T. R., Schultz, R. A., Robinson, M. S., & Cook, A. C. (2002). The mechanical and thermal structure of mercury's early lithosphere. *Geophysical Research Letters*, *29*, 37-1-37-4.

Watters, T. R., Solomon, S. C., Robinson, M. S., Head, J. W., Andre, S. L., Hauck, S. A., & Murchie, S. L. (2009). The tectonics of mercury: The view after messenger's first flyby. *Earth and Planetary Science Letters*, *285*, 283-296.

Xie, J., zhang, m., & Huang, C. (2022). Influence of megaregolith on the thermal evolution of mercury's silicate shell. *Research in Astronomy and Astrophysics*. Retrieved from http://iopscience.iop.org/article/10.1088/1674-4527/ac4ca1

XieJChris. (2022, January). *XieJChris/Formation-thrust-faults-in-Mercury-NSP: NSP-V2.0.* Zenodo. Retrieved from https://doi.org/10.5281/zenodo.5912132 doi: 10.5281/zenodo.5912132

Zhong, S., & Watts, A. B. (2013). Lithospheric deformation induced by loading of the hawaiian islands and its implications for mantle rheology. *Journal of Geophysical Research*, *118*, 6025-6048.

Zuber, M. T., Montési, L. G. J., Farmer, G. T., Hauck, S. A., Ritzer, J. A., Phillips, R. J., ... Johnson, C. L. (2010). Accommodation of lithospheric shortening on mercury from altimetric profiles of ridges and lobate scarps measured during messenger flybys 1 and 2. *Icarus*, *209*, 247-255.

Zuza, A. V., Levy, D. A., & Mulligan, S. R. (2020). Geologic field evidence for non-lithostatic overpressure recorded in the north american cordillera hinterland, northeast nevada. *Geoscience Frontiers*.